



Unidirectional particle transport in microfluidic chips operating in a tri-axial magnetic field for particle concentration and bio-analyte detection

Negar Sadeghidelouei¹ · Roozbeh Abedini-Nassab¹

Received: 22 August 2023 / Accepted: 28 November 2023 / Published online: 24 December 2023
© The Author(s), under exclusive licence to Springer-Verlag GmbH Germany, part of Springer Nature 2023

Abstract

The Controlled transport of tiny particles in a microfluidic environment has attracted the attention of numerous researchers in the field of lab-on-a-chip. In this work, for the first time, a fully operational microfluidic chip composed of asymmetric magnetic tracks that unidirectionally transport multiple magnetic particles synced with a general tri-axial magnetic field is proposed. In this innovative chip, the particle motion is analogous to the electron transport in electrical diodes, with similar controllability and automation levels not seen in other single-particle manipulation systems. The vertical bias component of the magnetic field by providing a repulsive force between the particles and preventing undesired cluster formation, makes the proposed chip even more similar to the electrical circuits. Additionally, the chip functions as a highly sensitive biosensor capable of detecting extremely low levels of DNA fragments using ligand-functionalized magnetic beads. The uniqueness of the proposed sensor lies in the introduction of a novel particle/analyte concentrator based on the proposed diodes, which enhances its detection sensitivity. This sensitivity is even further enhanced by a single-particle and pair detection image processing code. Furthermore, the background noise is reduced by eliminating the unwanted bead cluster formation commonly observed in previous works. The proposed device serves as a high-throughput unidirectional transport system at the single-particle resolution, offering sensitive bio-detection with many applications in biomedicine.

Keywords Unidirectional particle transport · Magnetophoretic transport · Finite element methods · Microfluidic · Lab on a chip · Concentrator · Biosensor

1 Introduction

Single particle (e.g., cell or bead) manipulation is a crucial task in the lab-on-a-chip (LOC) field, the importance of which in biology and bioengineering is obvious. This field has a great impact on various applications including cancer treatment (Abonnenc et al. 2013), drug invention and drug delivery (Roichman et al. 2007; Kang et al. 2008; Dittrich and Manz 2006; Nguyen et al. 2013), detecting viruses (Abonnenc et al. 2013), particle separation, and clinical diagnostics based on acoustic forces (Abedini-Nassab et al. 2021; Connacher et al. 2018; Ohiri et al. 2018), optical tweezers (Roichman et al. 2007; Ashkin 1997; Block et al. 1990;

Xiao and Grier 2010; Pelton et al. 2004; Ladavac et al. 2004; Chiou et al. 2005), hydrodynamic flows (Skelley et al. 2009; Carlo et al. 2007; Kuntaegowdanahalli et al. 2009; Herzenberg et al. 2002), dielectrophoretic forces (DEP) (Pesch and Du 2021; Punjiya et al. 2019; Abedini-Nassab et al. 2022), microengraving (Love et al. 2006; Han et al. 2010), flow cytometry (Gnyawali et al. 2019), and droplet-based microfluidics (Mantri et al. 2021; Macosko et al. 2015; Samlali et al. 2020). For example, it is now widely known that cell heterogeneity in cancer tumors plays a key role in disease development (Cha and Lee 2020; Wu et al. 2021; Lawson et al. 2018). Hence, researchers need novel single-cell analysis tools capable of precise manipulation of single cells and individual beads to detect cell behavior with single-cell resolution. Such crucial information is not easily detectable with the traditional bulk-level analysis methods (Sande et al. 2023; Luo, et al. 2022).

The available particle manipulation techniques have their own advantages and disadvantages. In method based on

✉ Roozbeh Abedini-Nassab
abedini@modares.ac.ir

¹ Faculty of Mechanical Engineering, Tarbiat Modares University, P. O. Box, Tehran 14115-111, Iran

hydrodynamic flows (Skelley et al. 2009; Carlo et al. 2007; Kuntaegowdanahalli et al. 2009; Herzenberg et al. 2002), microengraving (Love et al. 2006; Han et al. 2010), or acoustic forces (Abedini-Nassab et al. 2021; Connacher et al. 2018; Ohiri et al. 2018), control over individual particles is not offered. In methods based on optical tweezers (Roichman et al. 2007; Ashkin 1997; Block et al. 1990; Xiao and Grier 2010; Pelton et al. 2004; Ladavac et al. 2004; Chiou et al. 2005), precise control over individual particles is achieved; however, they are considered expensive methods, and their potential damaging impacts are reported (Volpe et al. 2023; Blázquez-Castro 2019).

Methods based on magnetophoretic forces are considered promising candidates for remotely manipulating particles in microfluidic systems (Abedini-Nassab and Eslamian 2014; Huergo et al. 2021; Lefebvre, et al. 2020). To answer this need, in recent years, we have developed magnetophoretic circuits composed of circuit elements similar to those found in electronic circuits, including conductors, transistors, and diodes. Analogous to electronic circuits that conduct numerous electron currents simultaneously, the magnetophoretic circuits enable the precise control of magnetic particle trajectories in a highly parallel manner. These chips are constructed using magnetic thin films engineered to achieve the desired energy distribution for effective particle manipulation in an externally applied rotating magnetic field.

The initial version of the magnetophoretic circuits operates in an in-plane two-dimensional (2D) external magnetic field (Lim et al. 2014; Abedini-Nassab et al. 2015; Abedini-Nassab 2019). But, to prevent particle cluster formation, which may halt the device operation, the next version of the magnetophoretic circuits, operating in a three-dimensional (3D, hereafter called tri-axial) field, is introduced (Abedini-Nassab and Shourabi 2022; Abedini-Nassab and Bahrami 2021a). This tri-axial field (See Fig. 2c) is composed of an in-plane rotating field and a vertical bias component. The rotating field component is generated by arranging four coils (numbered 1 in Fig. 1b) around the chip, while the vertical component is added by placing the fifth coil (numbered 2 in Fig. 1b) underneath the chip. The inclusion of the vertical bias magnetic field provides a repulsive force between particles, preventing particle nucleation. This phenomenon has been discussed elsewhere (Abedini-Nassab and Shourabi 2022); however, in short, in an in-plane field, the particles are biased in such a way that their opposite (i.e., north and south) poles are directed toward each other. Hence, they experience an attractive force (See Fig. 1i). However, in a tri-axial magnetic field, the vertical bias component alters this arrangement, causing the opposite poles to not meet (See Fig. 1j).

Although the conductors and transistors operating in tri-axial fields are fully studied (Abedini-Nassab and Shourabi 2022; Abedini-Nassab et al. 2016), the diodes

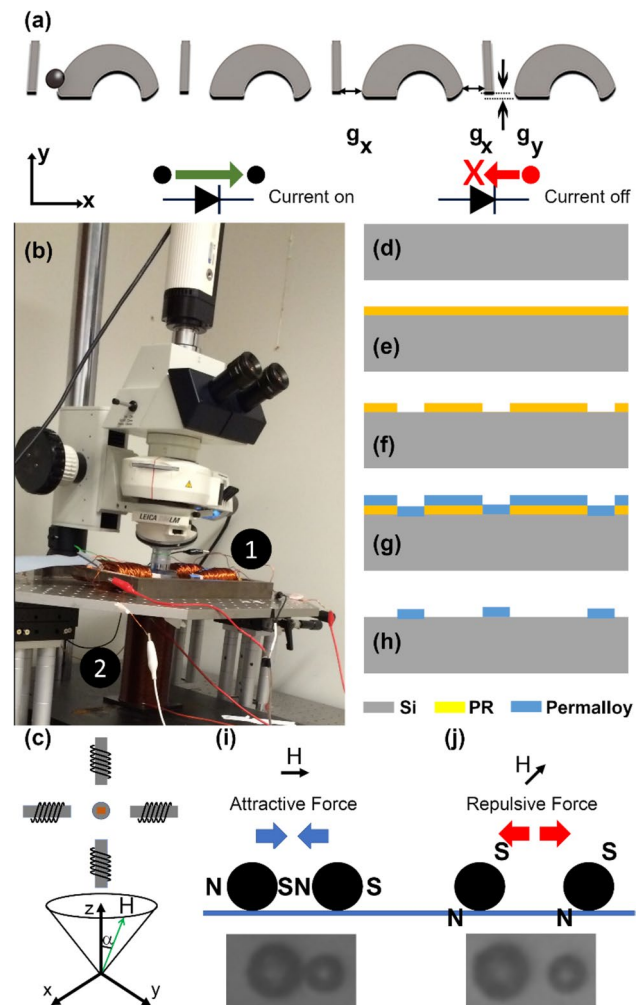


Fig. 1 **a** A 3D illustration of the proposed diode is shown. The diode transports the particles in the forward mode (green arrow) but not in the reverse bias (red arrow). **b** The experimental setup is illustrated. Number 1 shows the four coils around the chip producing the in-plane rotating component of the magnetic field, and number 2 depicts the coil producing the vertical component of the magnetic field. **c** Schematic of the magnetic field setup is shown (top view). The four coils are sitting around the chip and the fifth one is placed underneath the chip (light brown rectangle). The produced tri-axial magnetic field with cone angle α is shown with the green arrow (H). **d–h** The fabrication steps are depicted. **c** Starting from a silicon wafer, **d** a negative photoresist (PR) covers the chip, **e** which is patterned after photolithography. **f** The chip is covered with permalloy. **g** After lift-off, the permalloy layer is patterned. **i** In an in-plane field, an attractive force forms between magnetic particles. Both schematic and experimental pictures are shown. **j** In a tri-axial field, a repulsive force forms between magnetic particles. Both schematic and experimental pictures are shown. H stands for the magnetic field direction, and the blue rectangle depicts the substrate (color figure online)

are not characterized yet. In this work, finite element methods (FEM) are used to analyze the energy distribution on this device, based on which the particle trajectories are predicted. The simulation predictions are validated with the experimental data. It is shown that the proposed

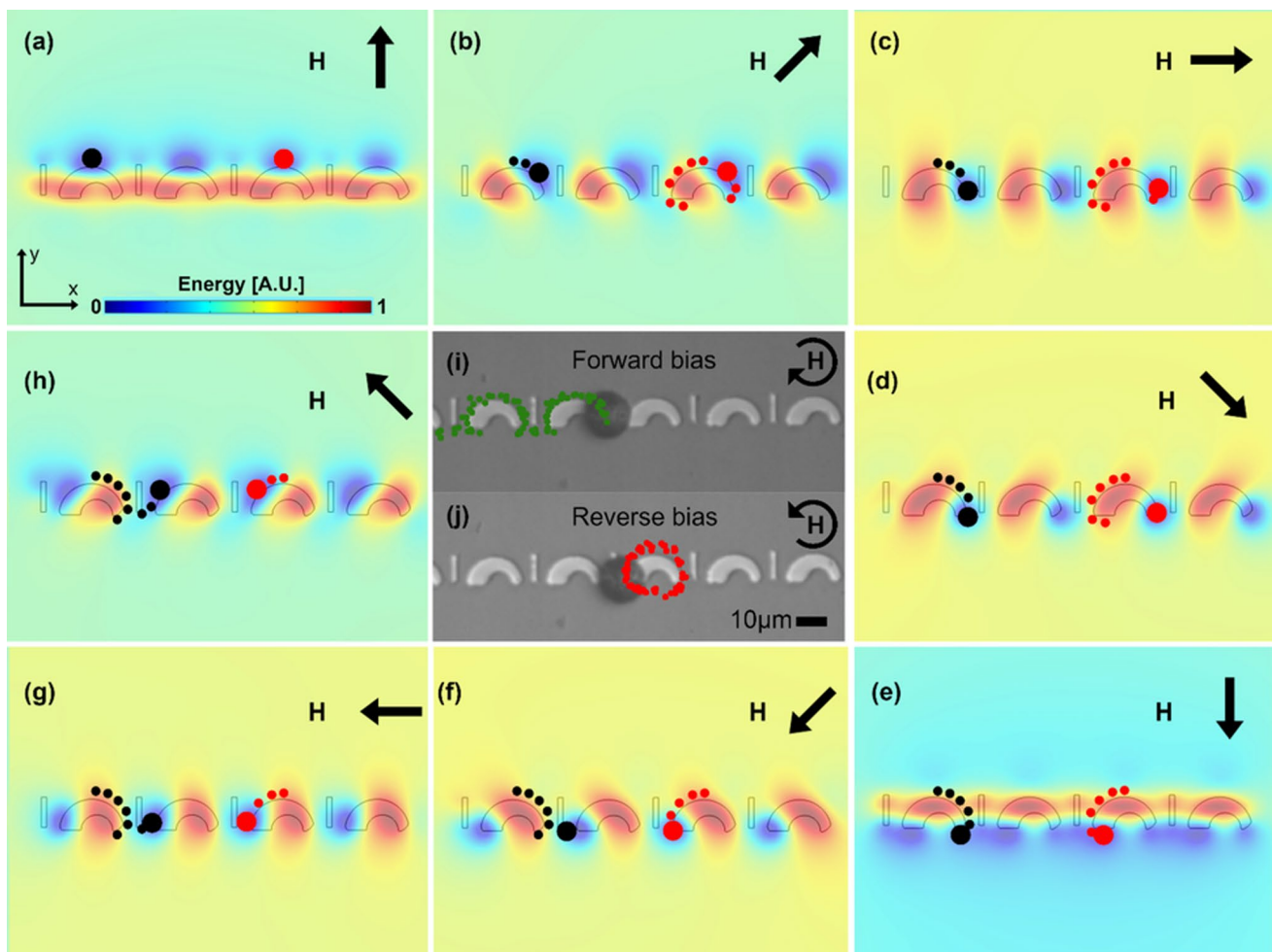


Fig. 2 The energy simulation results for the proposed diode for a complete cycle with steps of 45° and the experimental observations are illustrated. **a-h** The energy landscapes are produced by FEM simulations. The black arrows depict the in-plane field directions. The blue and red areas stand for the regions with low and high magnetic energies, respectively. The small black circle represents a parti-

cle, and the dotted line depicts the particle trajectory. **i, j** The diodes operating in **i** forward and **j** reverse bias are illustrated. The green and red dots in **i** and **j** represent the overlaid experimentally observed trajectories of particles in forward and reverse bias modes, respectively. The circular arrows in **i, j** depict the direction of the in-plane component of the externally applied magnetic field (color figure online)

geometry transports the particles in one direction, but not in the reversed external magnetic field (See Fig. 1a). This behavior is similar to the diodes in electrical circuits that conduct electrical currents in one direction but not in the reverse bias. In this work, various device design parameters are carefully studied, and the effect of particle size is investigated.

In the proposed magnetophoretic circuits, the width of the magnetic tracks for manipulating particles is $\sim 10\text{--}15\ \mu\text{m}$. Thus, on a $75 \times 25\ \text{mm}^2$ chip (i.e., the size of a typically used glass slide), a hundred magnetic tracks, each capable of transporting 100 cells, can be easily fabricated. Consequently, the chip can easily manipulate $\sim 10,000$ particles simultaneously. Importantly, all particles move synched with the external magnetic field without requiring control signals for individual particles.

Biosensing is an important need in the field of biology to be answered with lab-on-a-chip tools. For example, simplex virus type 1 (HSV-1, or oral herpes) is a DNA virus belonging to the Herpesviridae family that affects more than 60% of the global population. Culture-based or polymerase chain reaction-based diagnosis methods are used currently; however, the field needs more sensitive HSV diagnostic tools (Arshad et al. 2019). Here, for the first time, a chip based on the proposed magnetophoretic diode design is introduced to detect low levels of HSV-1. This need is answered by first concentrating the analyte-carrying particles at the center of the chip. The analyte concentration after accumulation increases so that it can be detected more easily. Then, analytes between the ligand-functionalized magnetic beads making bead pairs with an image-processing code are detected. By applying a vertical field to the chip, a repulsive

force is provided between the unpaired beads (i.e., the beads with no analyte), decreasing the sensor background noise. This work shows the capability of this sensitive sensor to detect ultra-low levels of DNA that have not been achieved in previous studies (Rampini et al. 2021).

In the rest of this study, first, the theory and methods used for investigating the operation of the device are introduced. Next, the results are presented and then discussed. Then, the capability of the chip to concentrate the particles at the center of the chip is presented. Also, a highly sensitive single-molecule detection assay based on the proposed design is demonstrated. The studied diode and its identified design parameters are crucial in designing the integrated magnetophoretic circuits with fundamental applications in biology and medicine.

2 Materials and Methods

2.1 Theory and simulations

The magnetic force applied on a magnetic particle in a magnetic energy distribution is calculated as shown in Eq. (1):

$$\vec{F} = -\nabla U \quad (1)$$

where U is the magnetic energy. This equation shows that the magnetic particles tend to move to the spots with minimum energies (i.e., the energy wells). In this work, COMSOL software is used to run FEM simulations to obtain the energy distribution around the magnetic thin films. Then, by plugging the obtained energy in Eq. (1), the magnetic force on the magnetic particles is calculated.

The magnetic microparticles in a magnetic field can be treated as point dipoles. In aqueous fluids, their movement can be modeled with overdamped first-order equations of motion. The particle velocity is calculated by the Stokes force on spherical particles:

$$\vec{v} = \frac{\vec{F}_D}{6\pi\eta r} \quad (2)$$

where F_D , η , r , and v are the drag force, fluid viscosity, particle radius, and particle velocity, respectively. At the steady state, the magnetic and the drag forces are equal. Thus, by plugging the calculated force from Eq. (1) into Eq. (2), the particle velocity is obtained. Then, the particle trajectory is determined by using a simple forward difference scheme:

$$\vec{r}_i = \vec{r}_{i-1} + \vec{v}_{i-1} \Delta t \quad (3)$$

where r and Δt stand for the particle position and the time step, respectively. Based on Eq. (3), the particle position is determined based on its position at the previous step and

its velocity. A proper time step, Δt , is required to achieve an optimized computation time and numerical convergence simultaneously.

In this work, the magnetophoretic diode geometries were designed in AutoCAD and then imported into COMSOL software. In COMSOL, a 3D component, the magnetic fields physics, and the stationary study were used. By choosing a good mesh (minimum element size and maximum element size were 0.0182 μm and 1.82 μm , respectively, with mesh quality higher than 0.5) the solution was converged. After computation, the energy landscape data was exported to be used in force and velocity studies.

2.2 Experimental methods

The fabrication steps are demonstrated in the schematic in Fig. 1c–g. The process is explained elsewhere (Abedini-Nassab and Emamgholizadeh 2022). But briefly, silicon wafers (University Wafer, Boston, MA, USA) were cleaned with acetone and isopropanol and dried with nitrogen gas (See Fig. 1c). Then, they were spin-coated with negative photoresist (NFR16-D2 JSR Micro Inc., Sunnyvale, CA) for 5 s at 500 revolutions per minute (RPM), followed by 30 s at 3000 RPM (Headway spinner). Then, they were pre-baked at 90 °C for 60 s on a hotplate (See Fig. 1d). Next, they were exposed to ultraviolet (UV) light for 12 s at an illumination power of 13.5 mW with a wavelength of 365 nm (Karl Suss MA6/BA6). Then, the chips were post-baked at 90 °C for 60 s on the hotplate. Next, the patterns were developed using Microposit MF-319 developer (Shipley, Marlborough, MA) by placing the chips in it for 60 s. Then, the chips were rinsed with deionized water and dried with nitrogen gas (See Fig. 1e). After O_2 plasma ashing for 60 s at 100mW, the chips were ready for the metal evaporation step. Using an electron-beam evaporating system (Kurt Lesker PVD 75) a 5/100 nm thick stack of $\text{Ti}/\text{Ni}_{80}\text{Fe}_{20}$ film was deposited on top of the chips. The operating pressure was set to 1×10^{-5} (See Fig. 1f). To remove the excess metals using the metal lift-off technique, the chips were placed in 1165 resist remover (NMP) at 65 °C and kept for 5 min (See Fig. 1g). After being rinsed with acetone and isopropanol, the chips were dried with nitrogen gas and became ready to be coated with an insulating layer. This step was done by depositing a 200 nm thick layer of SiO_2 , using the Plasma Enhanced Chemical Vapor Deposition (PECVD) method (Advanced Vacuum Vision 310) at 250 °C, at a rate of 40nm/s.

A microscopy stage equipped with a camera (See Fig. 1b) was used to run the experiments. The chip was mounted under the microscope while five magnetic coils surrounded it (i.e., four coils (numbered 1 in Fig. 1b) were located in-plane with the chip, and the fifth coil (numbered 2 in Fig. 1b) was placed underneath the chip). Figure 1c illustrates a schematic of the coils (top view) and the produced tri-axial field.

In our experiments, we used Dynabeads M-280, Spherotech CM-50–10, and FCM-8056–2 with mean diameters of 2.8, 5.7, and 8.4 μm , respectively.

In the sensor experiments, the DNA fragments were labeled with biotin and digoxigenin oligonucleotide probes. This labeling allows them to bind in between streptavidin and anti-digoxigenin antibody-labeled magnetic beads.

3 Results and discussions

3.1 Unidirectional particle transport

Previous studies have demonstrated that curved geometries with a symmetric magnetic track transport the particles in both directions (i.e., it works as a conductor) (Abedini-Nassab and Emamgholizadeh 2022). Thus, to achieve a unidirectional transport (i.e., as a diode), a geometry without mirror symmetry is required. Therefore, the proposed magnetophoretic diode, illustrated in Fig. 1a, consists of curved magnets with one end wider than the other. To be consistent with the conductor design in previous works (Abedini-Nassab and Emamgholizadeh 2022), the I bar is added to the diode design. It has been shown that the I bar aids in holding and then transferring the particles to the next curved magnet (Abedini-Nassab and Emamgholizadeh 2022). Also, the longer distance between the two curved magnets in the design with the I bar compared to the design without it, enhances the overall particle transport speed. For example, at the frequency of 0.1 Hz, incorporating an I bar with a width of 2 μm and gaps of 3 μm between the magnets results in a particle velocity increase of 0.5 $\mu\text{m}/\text{s}$. Thus, although our simulation results (not presented here) indicate that the design without I bars works too, we chose to keep the I bar in the design.

When the externally applied magnetic field rotates in the clockwise direction (considering the design in Fig. 1), the magnetic particles in their proximity move in open trajectories along the magnetic track. We call this condition “forward bias” in analogy to the forward-biased diodes in electronic circuits. But when the magnetic field rotates counterclockwise, the magnetic particles move in closed trajectories, the condition which we call the “reverse bias”. The origin of this asymmetrical behavior of the device (i.e., transporting the particles in one direction but not in the reverse direction) comes from the deeper energy well appearing near the thicker segment of the track, compared to that of the narrower segment.

To carefully study this behavior, this work analyzes the energy distribution on this device, as shown in Fig. 2. A cone angle (i.e., the angle between the unit vector normal to the chip plane and the magnetic field) of $\alpha = 45^\circ$ consistent with the magnetophoretic conductors operating in a tri-axial

magnetic field presented previously (Abedini-Nassab and Shourabi 2022; Abedini-Nassab and Bahrami 2021b) is chosen (See Fig. 1c). The in-plane field component in Fig. 2 is shown by the black arrow in each panel. Starting from Fig. 2a, when the field direction is towards +y, the energy wells (blue regions) form on the +y side of the magnets. These areas are the spots to which magnetic particles tend to move to obtain minimum energy. By rotating the external field, the energy wells and the magnetic particles following them circulate the curved magnets in the clockwise direction until they reach the narrow segment of the curved magnets in Fig. 2e. Next, in Fig. 2f, the energy well on the narrow segment disappears, while the energy well on the I bar tip in the vicinity still exists. Thus, the particle which initially was transported to the narrow segment of the curved magnet, moves to the I bar tip. Similarly, in the next step, as shown in Fig. 2g, the energy well on the I bar tip disappears, and the particle moves to the energy well on the next circular magnet on the right. Hence, in one cycle of the external field rotation, the particle moves one magnetic track period forward. In Fig. 2, the black circle and the black dotted line at each panel show the position of the particle based on simulation results and the particle trajectory, respectively. Experimental particle trajectories are overlaid on the microscopy picture in Fig. 2i for the diode forward bias. Good agreement between the simulation predictions and the experimental results is observed.

To better understand the transition between the tips of the curved magnet and the I bar, an additional analysis with finer steps is performed, the results of which are presented in Fig. 3. In this figure, in addition to the magnetic energy distribution, the energies along two possible paths (i.e., forward and backward particle trajectories) are plotted. The reason for choosing these two paths is to find whether the particle initially located at point 2 moves toward the energy well at point 1 or to the one at point 3, along lines 1–2 and 2–3, in black and red, respectively. In Fig. 3a, the energy well is at the intersection of the two lines, indicating the particle is on the narrow segment of the curved magnet. At this step, the particle sees energy barriers on both sides. In the next step, by rotating the external magnetic field, the barrier in the +x direction disappears (See Figs. 3b, c), and the particle sees an energy slope towards point 3 on the I bar. Thus, the particle moves from the curved magnet to the I bar, which means the diode is operating in forward mode.

In Fig. 3d–f, points 1 and 3 are positioned on the left side of the wide section of the curved magnet and the right side of the I tip. Therefore, the energy plot in Fig. 3d includes the energy wells generated on these tips, which is consistent with the heatmap displayed in Fig. 3a. However, since this analysis focuses on the energy slopes adjacent to the initial position of the particle (e.g., point 2 in Fig. 3) as the key parameter defining particle movement, rather than the

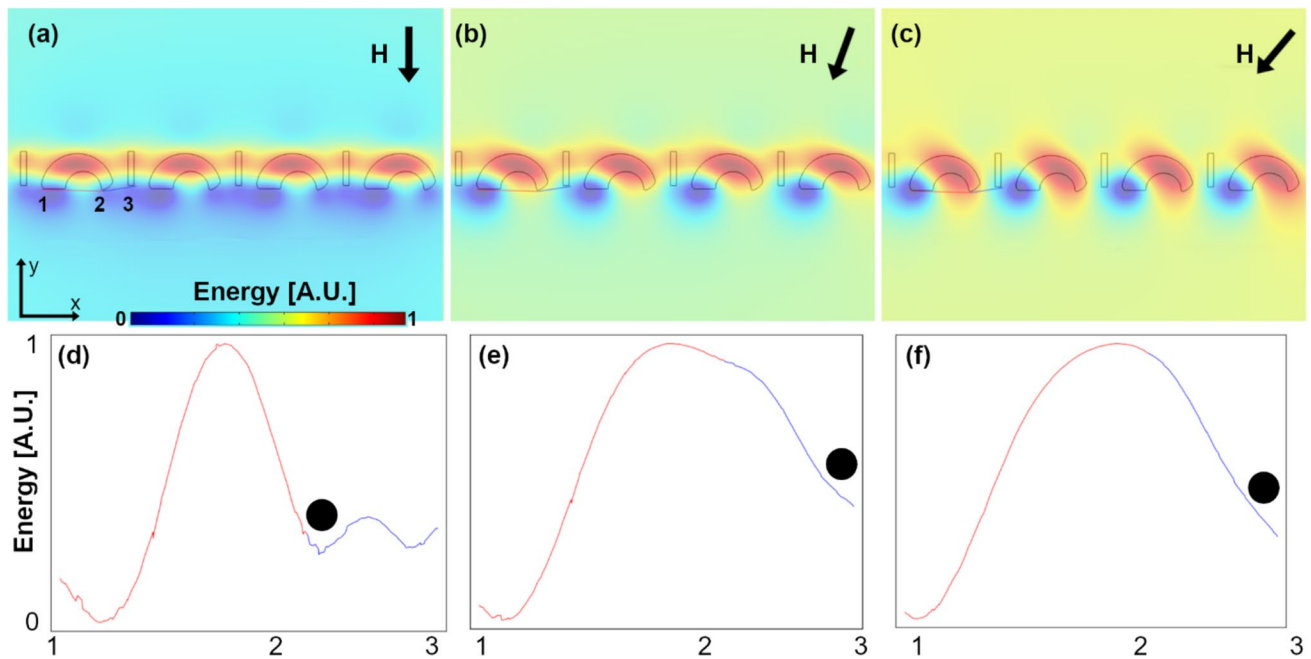


Fig. 3 The energy simulation results for the diode in forward bias mode. The black arrows depict the in-plane field direction at each panel. The field rotation step size in this figure is 20° . The energy landscapes are plotted in **a–c** and the corresponding energies along

the lines 1–2 and 2–3 are plotted in **d–f**, in red and blue, respectively. The blue and red areas stand for the regions with low and high energies, respectively. The black circle depicts the particle position at each field angle (color figure online)

wells at other points, and to maintain simplicity in the plots, we have limited the studied area in the subsequent figures. It means that we may not have included all the energy wells along the lines 1–2 and 2–3.

To study the diode in the reverse bias mode, the results in Fig. 2 in reverse order are considered. In this analysis, the energy wells and their follower particles circulate the curved magnets in the counterclockwise direction from their initial position in Fig. 2(a) toward $-y$ and $-x$ direction to reach the positions shown in Figs. 2h, g, f), and finally 2(e). At this point, the particles located at the wide segment of the curved shape see a deep energy on the narrow segment of the curved magnet and move to that spot (See Fig. 2d). Thus, the particles move in a closed orbit around the curved magnet. The red circle and the red dotted line in each panel of Fig. 2 represent the particle position based on simulations and its trajectory at each step, respectively. Experimental particle trajectories are overlaid on the microscopy picture in Fig. 2j for the reverse-biased diode. Good agreement between the simulation predictions and the experimental results is seen.

There is also an undesirable chance for the particles to move to the energy well on the I tip in the $-x$ direction. To gain a clearer understanding of this behavior (i.e., the particle transition between the wide and narrow segments of the curved magnet versus the transition between the curved and I magnets) more clearly, a study with a finer angle step (22.5°) is provided in Fig. 4, together with energy plots for each

energy landscape along the presented lines. In Figs. 4a, b, the energy well is located at the intersection of the two lines. It means the particle is on the wide segment of the curved magnet and is surrounded by energy barriers on both sides. In the next step, by rotating the external field, the barrier on the $+x$ direction lowers (See Figs. 4b, e and then disappears (See Figs. 4c, f). The particle sees a slope toward point 3 on the narrow segment of the curved magnet while it still sees the energy barrier toward point 1. Hence, it moves toward point 3, which means the diode works properly in the reverse bias mode.

To evaluate the capability of the device in manipulating particles of different sizes, simulations are performed at various heights (i.e., the center of the particles). In these simulations, each magnetic particle is treated as a point dipole located at the center of the particle. Based on our analysis, the device with a gap size and a disk outer diameter of 3 and 16 μm , respectively, can effectively manipulate the particles with radii in the range of 4–10 μm (the results are not shown). We also conducted simulations for particle radii smaller than 4 μm . For instance, Fig. 5 illustrates the energy simulation results for a particle with a radius of 3 μm . In this figure, the particle is initially located at point 2, which corresponds to the narrow segment of the curved magnet. At this position, two energy barriers on both sides prevent the particle from moving (See Fig. 5d). By rotating the external magnetic field, eventually, the two energy barriers disappear

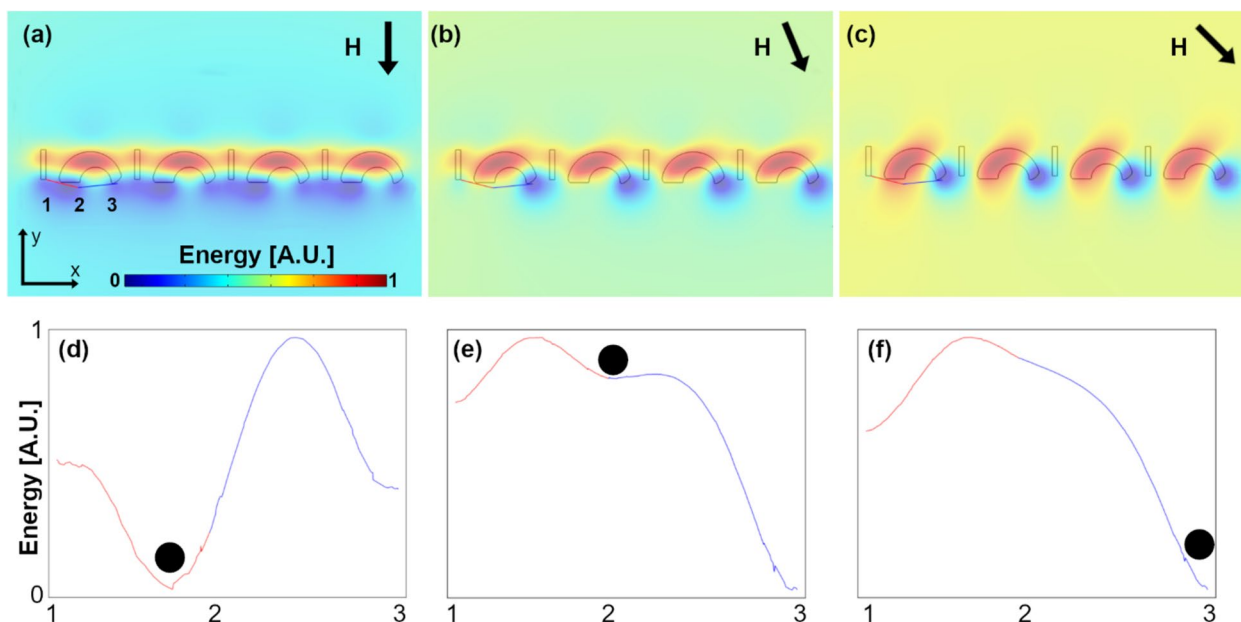


Fig. 4 The energy simulation results for the diode in the reverse bias mode. The black arrows depict the in-plane field direction in each panel. The energy landscapes are plotted in **a-c**, and the corresponding energies along the lines 1–2 and 2–3 are plotted in **d-f**, in red and

blue, respectively. The blue and red areas stand for the regions with low and high energies, respectively. The black circle depicts the particle position at each field angle (color figure online)

(See Fig. 5l), allowing the particle to move in any direction. In Fig. 5l, a small slope is seen toward the +x direction; however, the absence of a sufficient energy barrier in the -x direction does not guarantee proper device operation. After conducting these simulations and determining the proper particle size range, the particle radius of 4 μm was chosen for the rest of the simulations to investigate other parameters in the current work.

Another important parameter to consider is the gap between the magnets. Here, simulations for various gap sizes to analyze its impact are conducted. Based on our analysis (results not shown here), the I bar can be shifted in the +y direction by up to 5 μm, and the device can still efficiently transport the particles along the magnetic track. However, a 6 μm shift leads to an undesired particle transport (See Fig. 6), indicating that g_y must be kept lower than 6 μm.

In Fig. 6a, consider a particle initially positioned at the narrow segment of the curved magnet (point 2 in Fig. 6d). By rotating the magnetic field, a negative slope toward the I bar tip (point 3) is formed (See Fig. 6e). But even with further rotation of the external field, the energy barriers along the path do not disappear (See Figs. 6e–h). That means the particle cannot move properly along the desired path.

We also analyzed the effect of shifting the I bar in the -y direction (not shown here) and found that to achieve desired particle transports, this shift should be kept below 6 μm. Figure 6i illustrates our experimental results, demonstrating that a shift of 3 μm in +y for the I bar is acceptable, while

a 6 μm shift negatively impacts the device performance in particle transport.

Another important design parameter to consider is the gap between the magnets in the x direction (g_x). The initial gap size was 3 μm, which can be increased to 6 μm without affecting the proper functioning of the device. The simulation results of the design with $g_x = 6 \mu\text{m}$ (not presented here) show that it properly transports the particle. By contrast, Fig. 7 demonstrates that a diode design with $g_x = 7 \mu\text{m}$ does not operate effectively.

Assuming the particle is initially located at point 2 (See Fig. 7a, d, j), it observes an energy barrier in the +x direction even when the magnetic field rotates. The little energy barrier in Fig. 7e is shown by the red arrow. Hence, the device fails to move the particle to points 3–5. Our experimental results are plotted in Fig. 7i for particles with different sizes. These results also indicate that a shift in the +x direction of up to 3 μm is acceptable.

3.2 Particle concentration and analyte detection

After thoroughly studying the parameters of the proposed diode, we sought to demonstrate the feasibility of this unidirectional transport method to concentrate the target carrying beads to the center of a chip in two phases. As illustrated in the 3D schematic in Fig. 8a, the chip surface is covered with diodes connected perpendicularly to the two main diode paths in the center.

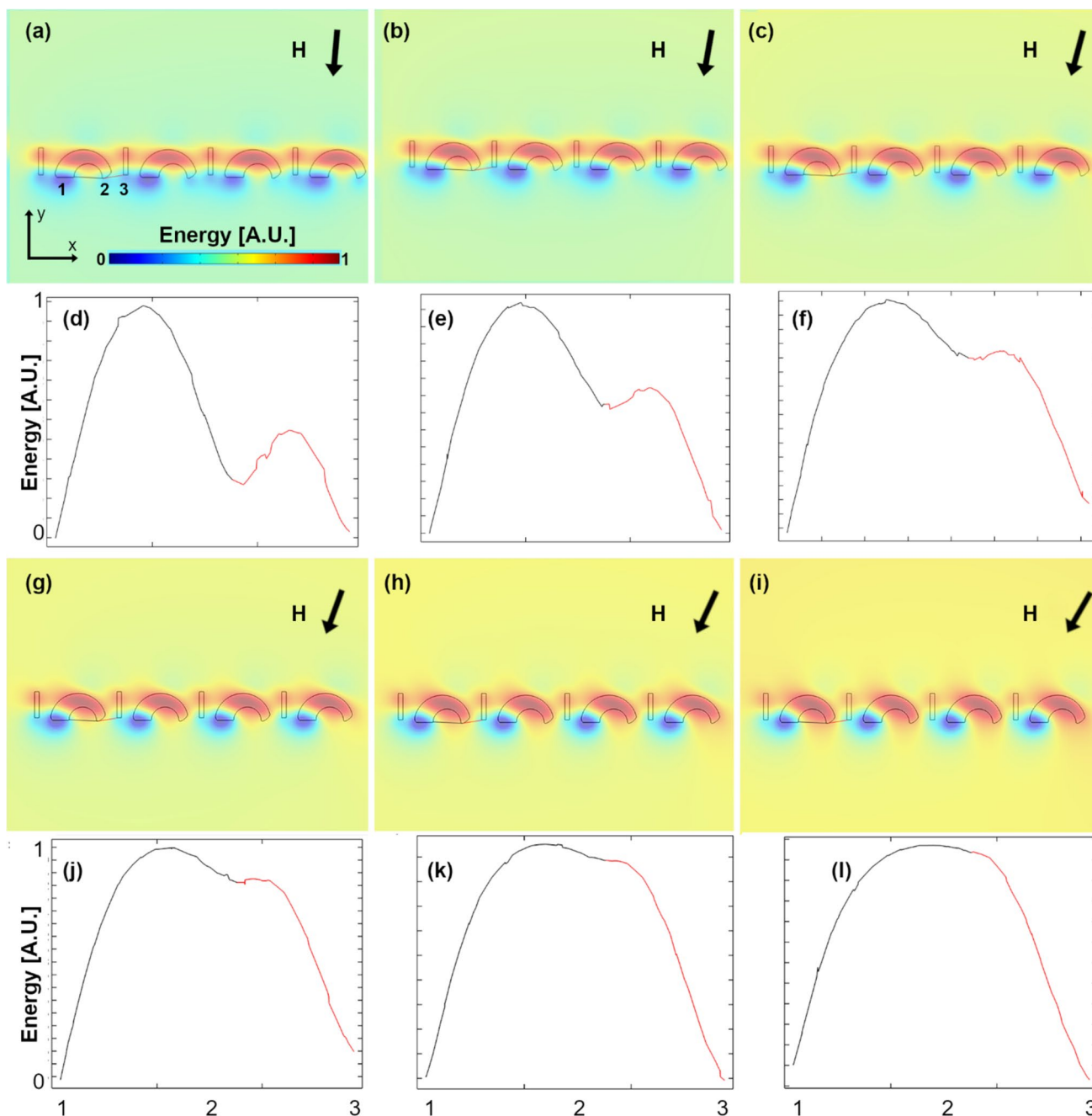


Fig. 5 Energy distributions for a particle with radius, gap size, and disk outer diameter of 3 μm , 3 μm , and 16 μm , respectively, are demonstrated. The energy landscapes are plotted in **a-c** and **g-i** and the corresponding energies along the lines 1–2 and 2–3 are shown in **d-f**

and **j-l**, in blue and red, respectively. The blue and red areas stand for the regions with low and high energies, respectively. The black arrows depict the in-plane field direction in each panel. The magnetic field rotation step size is 5° (color figure online)

In the first phase, by applying the external rotating magnetic field to the chip (clockwise), some diodes are forward-biased (e.g., diode 1), the particles on which move toward the main magnetic tracks located at the center of the chip (e.g., diode 2). In this phase, the other diodes are biased in reverse mode and do not transport the particles

(e.g., diode 3). Hence, in the first phase, the particle trajectory directions are toward the blue arrows in Fig. 8a.

Then, by inverting the magnetic field rotation in the second phase, the bias of all the diodes changes. In other words, the initially reverse-biased diodes switch to forward bias, enabling them to transport the particles toward the main

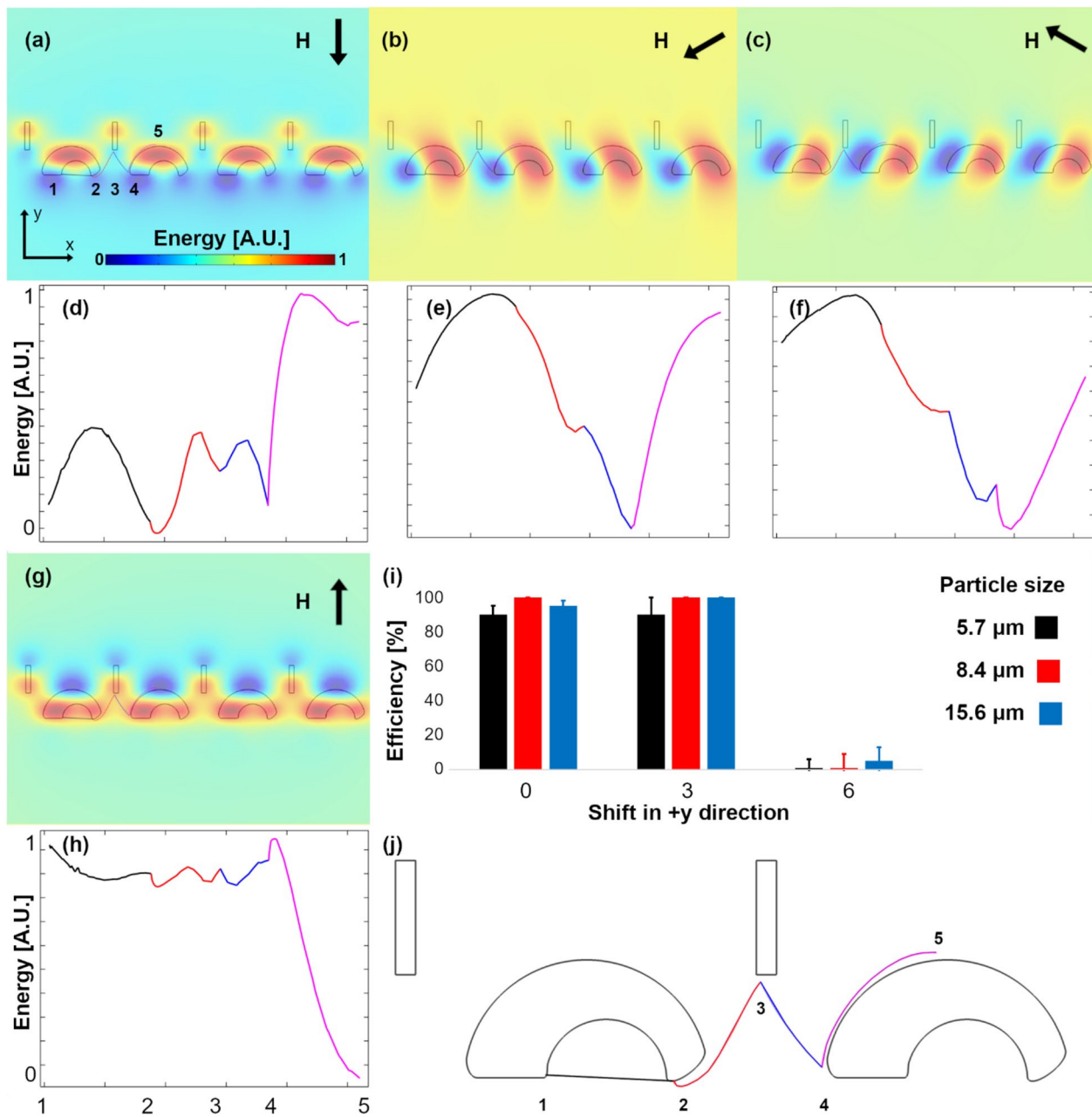


Fig. 6 Energy distributions for the design with shifting the I bar toward +y direction by 6 μm ($g_y = 6 \mu\text{m}$) are illustrated. The particle radius, the g_x , and the outer disk diameter are 4 μm, 3 μm, and 16 μm, respectively. The energy landscapes are plotted in **a–c** and **g** and the corresponding energies along the lines 1–2, 2–3, 3–4, and 4–5 are plotted in **d–f** and **h**, in black, red, blue, and magenta respectively. The blue and red areas in **a–c** and **g** stand for the regions with low

and high energies, respectively. The black arrows depict the in-plane field direction in each panel. The magnetic field rotation step size is 60°. **i** The experimental particle transport efficiencies for various particle sizes and for geometries with different shifts of the I bar in +y direction are plotted. **j** The important points for the energy plots are shown (color figure online)

magnetic tracks located at the center of the chip. The particle trajectory directions in this phase are toward the green arrows in Fig. 8a. Hence, eventually, the particles are collected at the center of the chip (the area in the green circle).

We also conducted simulations of the T junctions (i.e., the intersection of two perpendicular diodes). These

simulations demonstrated that the particle is effectively transported from one magnetic track to the other one (See Fig. 8d–f for the energy landscape simulation and Figs. 8g–i for the energy simulation along the 1–2, 2–3, and 3–4 cutlines, depicted in Fig. 8d).

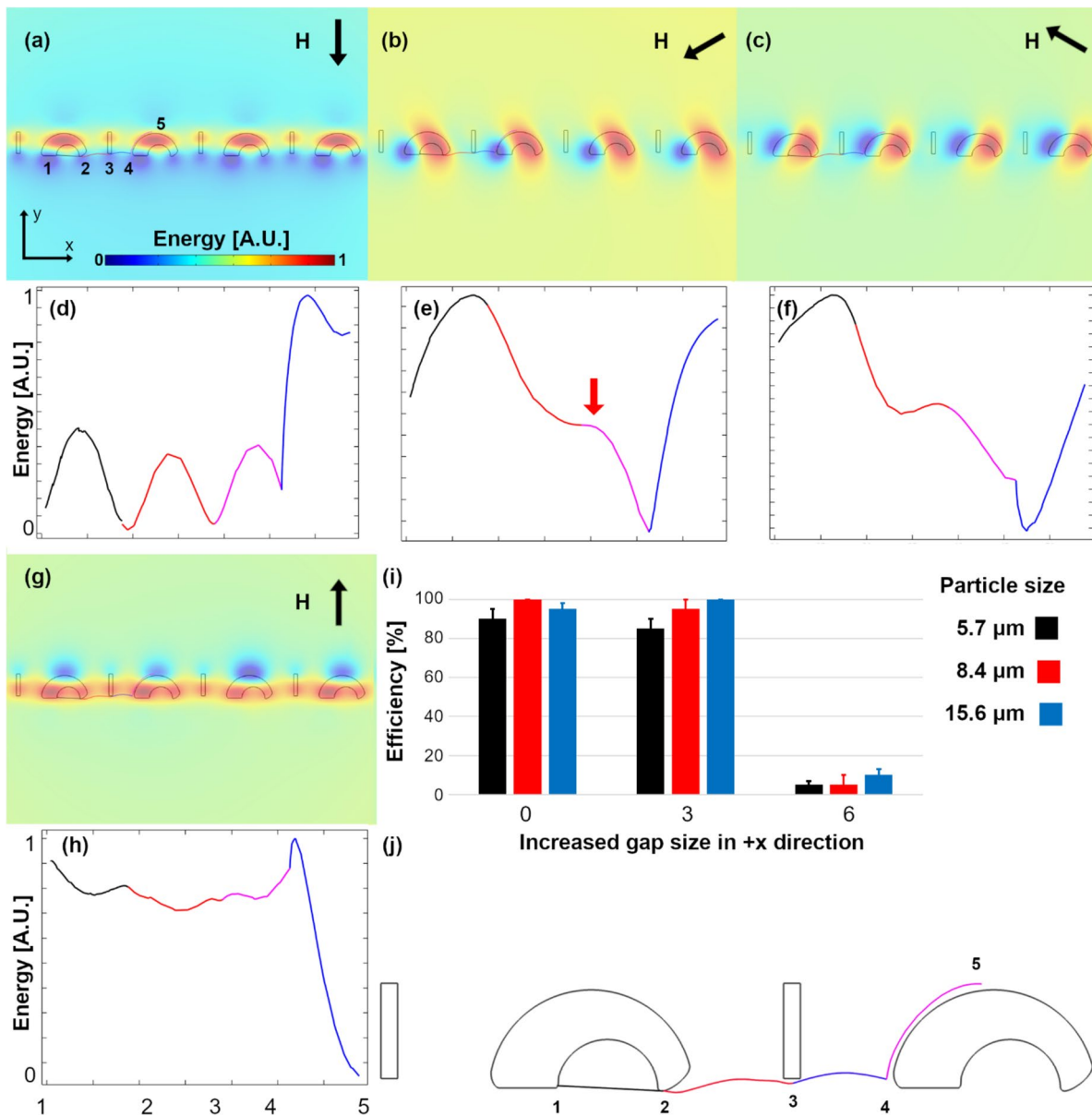


Fig. 7 Energy distributions for the design with $g_x=6\ \mu\text{m}$ are illustrated. The particle radius and the outer disk diameter are $4\ \mu\text{m}$ and $16\ \mu\text{m}$, respectively. The energy landscapes are plotted in **a–c** and **g** and the corresponding energies along the lines 1–2, 2–3, 3–4, and 4–5 are plotted in **d–f** and **h**, in black, red, blue, and magenta respectively. The blue and red areas in **a–c** and **g** stand for the regions with

low and high energies, respectively. The black arrows depict the in-plane field direction in each panel. The magnetic field rotation step size is 60° . **i** The experimental particle transport efficiencies for various particle sizes and geometries with increased gap size in the $+x$ direction are plotted. **j** The important points for the energy plots are shown (color figure online)

Here, the proposed method is used to concentrate the bio-targets (e.g., HSV-1 (Arshad et al. 2019)) at the center of the chip to detect them with higher sensitivities. Towards this goal, the beads are initially dispersed all over the chip to bind to the target DNAs (HSV UL27 gene) and carry them to the chip center. At this area on the chip (green circle in Fig. 8a), a single-molecule detection assay is designed.

This assay relies on the reaction of the target DNA between two magnetic beads. Once the beads are

concentrated in the accumulation region, the vertical bias field is turned off, allowing the beads to come into contact in a pure in-plane field. This interaction leads to the formation of bead doublets or clusters, which indicates the presence of the target DNA (See Fig. 8b).

Subsequently, the vertical field is turned on again, separating the bead pairs that do not have analyte molecules between them. This action leaves only the linked bead pairs. The bead pairs are detected using a Matlab image processing

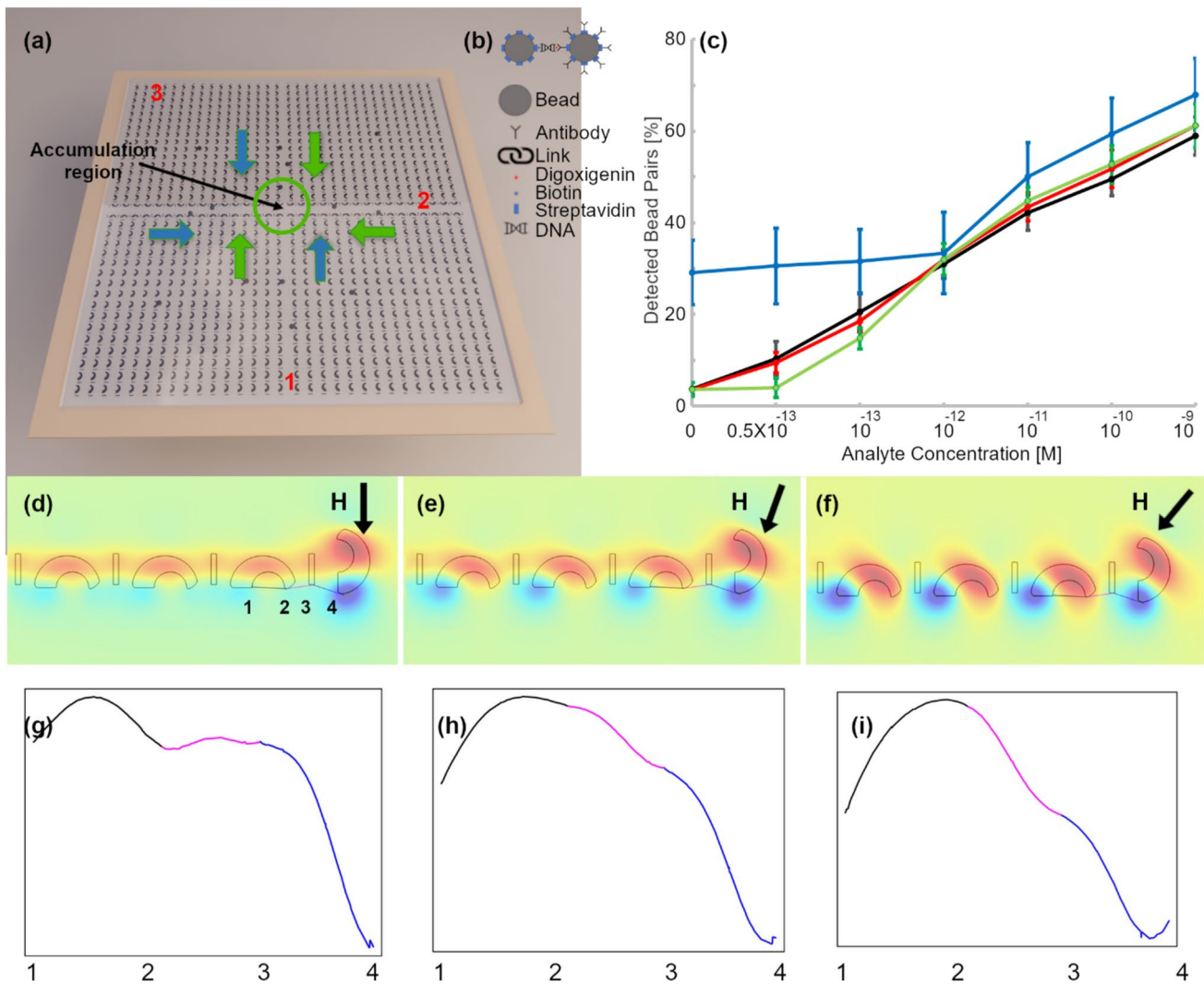


Fig. 8 Analyte concentrator and sensor based on the magnetophoretic diode. **a** Schematic of the chip covered with magnetophoretic diodes to concentrate the analyte-carrying particles to the center of the chip (i.e., accumulation region) in two operation phases. The blue and green arrows depict the particle trajectories in clockwise (first phase) and counterclockwise (second phase) magnetic field rotations, respectively. **b** In the accumulation region, the DNAs are linked between two particles forming particle pairs. These pairs are then detected with a Matlab code. **c** The bead pair percentage is plotted as a function of the HSV DNA concentration. The results obtained based on

the magnetophoretic circuits operating in a 3D magnetic field after being concentrated, the magnetophoretic circuits operating in a 3D magnetic field without any concentration step, magnetophoretic circuits operating in a 2D magnetic field, and flow cytometry are shown with red, green, blue, and black curves, respectively. **d–f** Energy distributions for the diode junction are shown. The black arrow in each panel depicts the magnetic field direction. The magnetic field angle step is 20°. **g–i** The energy distribution along lines 1–2, 2–3, and 3–4 are plotted in the magnetic field directions shown in **d–f**, respectively (color figure online)

code by identifying beads and checking whether the distance between the two beads is equal to or less than the sum of their radii. The accuracy of the code in distinguishing single particles from particle pairs or clusters has been confirmed to be higher than 99.9%. Also, after applying the vertical bias field, 619 out of 623 magnetic bead pairs with no analyte linkage were successfully separated, indicating a separation efficiency higher than 99.35%.

In Fig. 8c, the relation between the number of detecting bead pairs and the concentration of the analyte in the

sample of interest is shown. This relationship is validated using FACS (Fluorescence-Activated Cell Sorting) measurements, as indicated by the comparison between the black and red curves. The results before analyte concentration are also shown (See the green curve). The blue curve in Fig. 8c shows the results of the experiments conducted in an in-plane magnetic field. Both the blue and green curves in this figure remain relatively flat at concentrations below 10^{-12} and 0.5×10^{-13} , respectively, which means the corresponding methods cannot detect analytes at those concentration

ranges. However, the red curve demonstrates that the method proposed in this work enables analyte detection at concentrations as low as 0.5×10^{-13} . This finding suggests that the proposed technique offers a significantly improved sensitivity compared to the other methods depicted by the blue and green curves.

The assay described in this work has two main advantages over the previously introduced similar methods (Abedini-Nassab and Shourabi 2022; Rampini et al. 2021). (i) It achieves a better sensitivity by effectively concentrating the biotargets. (ii) The vertical component of the magnetic field generates a repulsion force between the particles, preventing them from forming undesired particle clusters formation. In contrast, devices operating in a pure in-plane magnetic field (Rampini et al. 2021) may experience issues with particle cluster formations. By incorporating the vertical magnetic field component, the chance of incorrectly quantifying bead pairs linked with the analytes of interest is lowered.

4 Conclusions

In this work, a magnetophoretic diode operating in a tri-axial magnetic field is thoroughly characterized. The energy distribution in the forward and reverse biases is studied, revealing the ability of the device to have particles moving in open and close trajectories that resembles the operation of electrical diodes. By combining simulation results with experimental observations, the effect of various parameters, including the gaps in the diode magnetic track design and the particle size were studied. We found that the proposed device operates effectively with particles of radii in the range of 4 to 10 μm . Additionally, the design is not too sensitive to the gap size in the magnetic track design. The I bar in the diode design can be shifted up to 5 μm in $\pm y$ directions, and the gap in the x direction can be as wide as 5 μm . This characteristic is significant as it shows the robustness of the device against fabrication errors, which is particularly important considering the challenges associated with fabricating small gaps.

Furthermore, this work demonstrated a practical application of the proposed magnetophoretic diode by designing an analyte (e.g., HSV samples) concentrator and detector chip. The chip concentrates the analyte-carrying beads to the center, where they link to the other beads. The vertical component of the magnetic field lowers the likelihood of null bead pair formation, thereby enhancing the reliability of the device. By counting the bead pairs, the concentration of analytes was estimated. The ability of the proposed device to detect analytes at concentrations as low as 0.5×10^{-13} was demonstrated. The proposed diodes, in combination with other magnetophoretic circuit elements, can also be used in designing other magnetophoretic circuits, with other

important applications in single-cell biology and biomedical engineering.

Acknowledgements The authors are thankful to Ms. Zahra Vatanchi for providing the 3D illustration in Fig. 8a.

Author contributions NS performed the simulations and prepared the initial manuscript draft. RA Managed the project, ran the experiments, and wrote the main manuscript text. All authors reviewed the manuscript before submission.

Data availability The data that support the findings of this study are available within the article.

Declarations

Conflict of interest The authors declare that they have no conflict of interest.

References

- Abedini-Nassab R (2019) Magnetomicrofluidic platforms for organizing arrays of single-particles and particle-pairs. *J Microelectromech Syst* 28(4):732–738
- Abedini-Nassab R, Bahrami S (2021a) Synchronous control of magnetic particles and magnetized cells in a tri-axial magnetic field. *Lab on a Chip*
- Abedini-Nassab R, Bahrami S (2021b) Synchronous control of magnetic particles and magnetized cells in a tri-axial magnetic field. *Lab Chip* 21(10):1998–2007
- Abedini-Nassab R, Emamgholizadeh A (2022) Controlled transport of magnetic particles and cells using C-shaped magnetic thin films in microfluidic chips. *Micromachines* 13(12):2177
- Abedini-Nassab R, Eslamian M (2014) Recent patents and advances on applications of magnetic nanoparticles and thin films in cell manipulation. *Recent Pat Nanotechnol* 8(3):157–164
- Abedini-Nassab R, Shourabi R (2022) High-throughput precise particle transport at single-particle resolution in a three-dimensional magnetic field for highly sensitive bio-detection. *Sci Rep* 12(1):6380
- Abedini-Nassab R et al (2015) Characterizing the switching thresholds of magnetophoretic transistors. *Adv Mater* 27(40):6176–6180
- Abedini-Nassab R et al (2016) Magnetophoretic transistors in a tri-axial magnetic field. *Lab Chip* 16(21):4181–4188
- Abedini-Nassab R, Emami SM, Nowghabi AN (2021) Nanotechnology and Acoustics in Medicine and Biology. *Recent Pat Nanotechnol*. <https://doi.org/10.2174/1872210515666210428134424>
- Abedini-Nassab R et al (2022) Quantifying the dielectrophoretic force on colloidal particles in microfluidic devices. *Microfluid Nanofluid* 26(5):38
- Abonnenc M et al (2013) Lysis-on-chip of single target cells following forced interaction with CTLs or NK cells on a dielectrophoresis-based array. *J Immunol* 191(7):3545–3552
- Arshad Z et al (2019) Tools for the diagnosis of herpes simplex virus 1/2: systematic review of studies published between 2012 and 2018. *JMIR Public Health Surveill* 5(2):e14216
- Ashkin A (1997) Optical trapping and manipulation of neutral particles using lasers. *Proc Natl Acad Sci* 94(10):4853–4860
- Blázquez-Castro A (2019) Optical tweezers: phototoxicity and thermal stress in cells and biomolecules. *Micromachines*. <https://doi.org/10.3390/mi10080507>
- Block SM, Goldstein LS, Schnapp BJ (1990) Bead movement by single kinesin molecules studied with optical tweezers. *Nature* 348(6299):348–352

- Cha J, Lee I (2020) Single-cell network biology for resolving cellular heterogeneity in human diseases. *Exp Mol Med* 52(11):1798–1808
- Chiou PY, Ohta AT, Wu MC (2005) Massively parallel manipulation of single cells and microparticles using optical images. *Nature* 436(7049):370–372
- Connacher W et al (2018) Micro/nano acoustofluidics: materials, phenomena, design, devices, and applications. *Lab Chip* 18(14):1952–1996
- Di Carlo D et al (2007) Continuous inertial focusing, ordering, and separation of particles in microchannels. *Proc Natl Acad Sci* 104(48):18892–18897
- Dittrich PS, Manz A (2006) Lab-on-a-chip: microfluidics in drug discovery. *Nat Rev Drug Discov* 5(3):210–218
- Gnyawali V et al (2019) Simultaneous acoustic and photoacoustic microfluidic flow cytometry for label-free analysis. *Sci Rep* 9(1):1585
- Han Q et al (2010) Multidimensional analysis of the frequencies and rates of cytokine secretion from single cells by quantitative microengraving. *Lab Chip* 10(11):1391–1400
- Herzenberg LA et al (2002) The history and future of the fluorescence activated cell sorter and flow cytometry: a view from Stanford. *Clin Chem* 48(10):1819–1827
- Huergo LF et al (2021) Magnetic bead-based immunoassay allows rapid, inexpensive, and quantitative detection of human SARS-CoV-2 antibodies. *ACS Sens* 6(3):703–708
- Kang L et al (2008) Microfluidics for drug discovery and development: from target selection to product lifecycle management. *Drug Discovery Today* 13(1–2):1–13
- Kuntaegowdanahalli SS et al (2009) Inertial microfluidics for continuous particle separation in spiral microchannels. *Lab Chip* 9(20):2973–2980
- Ladavac K, Kasza K, Grier DG (2004) Sorting mesoscopic objects with periodic potential landscapes: optical fractionation. *Phys Rev E* 70(1):010901
- Lawson DA et al (2018) Tumour heterogeneity and metastasis at single-cell resolution. *Nat Cell Biol* 20(12):1349–1360
- Lefebvre O, et al. (2020) Reusable embedded microcoils for magnetic nano-beads trapping in microfluidics: magnetic simulation and experiments. *Micromachines (Basel)* 11(3)
- Lim B et al (2014) Magnetophoretic circuits for digital control of single particles and cells. *Nat Commun* 5:3846
- Love JC et al (2006) A microengraving method for rapid selection of single cells producing antigen-specific antibodies. *Nat Biotechnol* 24(6):703–707
- Luo X et al (2022) Microfluidic compartmentalization platforms for single cell analysis. *Biosensors (Basel)* 12(2):58
- Macosko EZ et al (2015) Highly parallel genome-wide expression profiling of individual cells using nanoliter droplets. *Cell* 161(5):1202–1214
- Mantri M et al (2021) Spatiotemporal single-cell RNA sequencing of developing chicken hearts identifies interplay between cellular differentiation and morphogenesis. *Nat Commun* 12(1):1771
- Nguyen N-T et al (2013) Design, fabrication and characterization of drug delivery systems based on lab-on-a-chip technology. *Adv Drug Deliv Rev* 65(11–12):1403–1419
- Ohiri KA et al (2018) An acoustofluidic trap and transfer approach for organizing a high density single cell array. *Lab Chip* 18(14):2124–2133
- Pelton M, Ladavac K, Grier DG (2004) Transport and fractionation in periodic potential-energy landscapes. *Phys Rev E* 70(3):031108
- Pesch GR, Du F (2021) A review of dielectrophoretic separation and classification of non-biological particles. *Electrophoresis* 42(1–2):134–152
- Punjiya M et al (2019) A flow through device for simultaneous dielectrophoretic cell trapping and AC electroporation. *Sci Rep* 9(1):11988
- Rampini S et al (2021) Design of micromagnetic arrays for on-chip separation of superparamagnetic bead aggregates and detection of a model protein and double-stranded DNA analytes. *Sci Rep* 11(1):5302
- Roichman Y, Wong V, Grier DG (2007) Colloidal transport through optical tweezer arrays. *Phys Rev E* 75(1):011407
- Samlali K et al (2020) One cell, one drop, one click: hybrid microfluidics for mammalian single cell isolation. *Small* 16(34):e2002400
- Skelley AM et al (2009) Microfluidic control of cell pairing and fusion. *Nat Methods* 6(2):147–152
- Van de Sande B et al (2023) Applications of single-cell RNA sequencing in drug discovery and development. *Nat Rev Drug Discov* 22(6):496–520
- Volpe G et al (2023) Roadmap for optical tweezers. *J Phys Photon* 5(2):022501
- Wu F et al (2021) Single-cell profiling of tumor heterogeneity and the microenvironment in advanced non-small cell lung cancer. *Nat Commun* 12(1):2540
- Xiao K, Grier DG (2010) Sorting colloidal particles into multiple channels with optical forces: prismatic optical fractionation. *Phys Rev E* 82(5):051407

Publisher's Note Springer Nature remains neutral with regard to jurisdictional claims in published maps and institutional affiliations.

Springer Nature or its licensor (e.g. a society or other partner) holds exclusive rights to this article under a publishing agreement with the author(s) or other rightsholder(s); author self-archiving of the accepted manuscript version of this article is solely governed by the terms of such publishing agreement and applicable law.